Full length article

Magnetic targeting combined with active targeting of dual-ligand iron oxide nanoprobes to promote the penetration depth in tumors for effective magnetic resonance imaging and hyperthermia

Ling Chen [a,b,1], Yang Wu [c,1], Haoan Wu [a], Jianzhong Li [d], Jun Xie [e], Fengchao Zang [f], Ming Ma [a], Ning Gu [a,*], Yu Zhang [a,*]

[a] State Key Laboratory of Bioelectronics, Jiangsu Key Laboratory for Biomaterials and Devices, School of Biological Science and Medical Engineering & Collaborative Innovation Center of Suzhou Nano Science and Technology, Southeast University, Nanjing 210096, PR China
[b] Key Laboratory of Environmental Medicine Engineering of Ministry of Education, School of Public Health, Southeast University, Nanjing 210096, PR China
[c] Research Center of Clinical Oncology, Jiangsu Cancer Hospital & Jiangsu Institute of Cancer Research & Nanjing Medical University Affiliated Cancer Hospital, Nanjing 210009, PR China
[d] Department of Nephrology, The First Affiliated Hospital of Soochow University, Suzhou 215006, PR China
[e] School of Life Science, Jiangsu Normal University, Xuzhou 221116, PR China
[f] Jiangsu Key Laboratory of Molecular and Functional Imaging, Medical School, Southeast University, Nanjing 210096, PR China

ABSTRACT

The combination of multi-targeting magnetic nanoprobes and multi-targeting strategies has potential to facilitate magnetic resonance imaging (MRI) and magnetic induction hyperthermia of the tumor. Although the thermo-agents based on magnetic iron oxide nanoparticles (MION) have been successfully used in the form of intratumoral injection in clinical cure of glioblastoma, the tumor-targeted thermotherapy by intravenous administration remains challenging. Herein, we constructed a c(RGDyK)- and D-glucosamine-grafted bispecific molecular nanoprobe (Fe_3O_4@RGD@GLU) with a magnetic iron oxide core of size 22.17 nm and a biocompatible shell of DSPE-PEG2000, which can specially target the tumor vessel and cancer cells. The selection of c(RGDyK) could make the nanoprobe enter the neovascularization endotheliocyte through $\alpha_v\beta_3$-mediated endocytosis, which drastically reduced the dependence on the enhanced permeability and retention (EPR) effect in tumor. This dual-ligand nanoprobe exhibited strong magnetic properties and favorable biocompatibility. *In vitro* studies confirmed the anti-phagocytosis ability against macrophages and the specific targeting capability of Fe_3O_4@RGD@GLU. Then, the imaging effect and anti-tumor efficacy were compared using different targeting strategies with untargeted nanoprobes, dual-targeted nanoprobes, and magnetic targeting combined with dual-targeted nanoprobes. Moreover, the combination strategy of magnetic targeting and active targeting promoted the penetration depth of nanoprobes in addition to the increased accumulation in tumor tissue. Thus, the dual-targeted magnetic nanoprobe together with the combined targeting strategy could be a promising method in tumor imaging and hyperthermia through *in vivo* delivery of theranostic agents.

Statement of Significance

Magnetic induction hyperthermia based on iron oxide nanoparticles has been used in clinic for adjuvant treatment of recurrent glioblastoma. Nonetheless, this application is limited to intratumoral injection, and tumor-targeted hyperthermia by intravenous injection remains challenging. In this study, we developed a multi-targeted strategy by combining magnetic targeting with active targeting of dual-ligand magnetic nanoprobes. This combination mode acquired optimum contrast imaging effect through MRI and tumor-suppressive effect through hyperthermia under an alternating current magnetic field. The design of the nanoprobe was suitable for targeting most tumor lesions, which enabled it to be an effective theranostic agent with extensive uses. This study showed significant enhancement of the penetration depth and accumulation of nanoprobes in the tumor tissue for efficient imaging and hyperthermia.

* Corresponding authors.
  E-mail addresses: guning@seu.edu.cn (N. Gu), zhangyu@seu.edu.cn (Y. Zhang).
[1] These authors contributed equally to this work.

1. Introduction

Magnetic iron oxide nanoparticles (MIONs) have been approved for use in clinic for decades owing to their strong magnetic properties and favorable biocompatibility. The first MION-based product named Feridex® was approved for use in 1996 as a T_2 contrast agent for MRI of liver disease [1]. MIONs can be used not only as a diagnostic agent but also as a therapeutic agent. In 2009, the dextran-modified MION with the trade name Feraheme® (ferumoxytol injection) was approved as an iron agent for the treatment of iron-deficiency anemia in chronic kidney disease (CKD) [2–4]. In recent years, NanoTherm® of MagForce Nanotechnologies GmbH was permitted for clinical treatment of recurrent malignant glioma through magnetic induction hyperthermia. Although this advancement brings large hope for further clinical applications of MION-induced thermotherapy [5], there remain challenges, especially for hyperthermia through intravenous administration of thermo-agents.

Hyperthermia is called green therapy for adjuvant treatment of advanced tumor in addition to chemotherapy, radiotherapy, and immunotherapy. As compared to conventional microwave- and radiofrequency-based ablation, which is invasive and harmful to the body tissues because of the inflammatory response, MION-induced mild hyperthermia is more advantageous [6,7]. Mild hyperthermia often refers to an increase in the temperature of the tumor to 39–42 °C, thereby inducing apoptosis of cancer cells, which are more susceptible to high temperature than healthy cells [8]. Owing to the key challenges of the systemic delivery of MIONs, which results in damage to off-target organs (such as liver and spleen) due to the heat produced, and limited MION accumulation in the targeted tumor region, some studies of magnetic induction hyperthermia have been limited to intratumoral injection of thermo-agents for the treatment of breast cancer, pancreatic cancer, glioblastoma, or epidermoid carcinoma [9–12]. Presently, the NanoTherm® is administered as an *in situ* injection in glioblastoma hyperthermia. However, tumor prognosis could not be monitored by MRI owing to the extremely high concentration of the NanoTherm® injection [13]. In addition, this method of direct perfusion may result in leakage of nanoparticles and heterogeneous distribution of heat in the tumor region.

It is worth noting that on reaching the tumor tissue, MIONs should generate adequate heat to achieve the treatment temperature. Hence, two major tasks need to be addressed: one is the amount of thermo-agents accumulated at the target site and the other is their heating power under a safe alternating current magnetic field (ACMF). Fortunately, the magnetic properties of MIONs are remarkably elevated with the development of the thermal decomposition method, which makes it possible to realize intravenously administrated delivery of thermo-agents to the tumor site. On the other hand, it is crucial to increase the intratumoral accumulation of MIONs as much as possible. Presently, passive targeting based on the EPR effect is the main way for the *in vivo* drug delivery of most nanomedicines. However, the distribution of nanoagents is diverse because of the heterogeneity of the EPR effect in the tumor [14,15], and the cumulant is also limited. The construction of a targeted nanoprobe is an effective method to simultaneously enhance the imaging sensitivity and improve the targeting efficacy. Furthermore, the dual-targeted nanoprobes were proved to be more sensitive in the detection of metastatic lesions than the single-targeted ones [16–19]. The drug-delivery systems with dual ligands were also reported to have deep penetration in the tumor and an enhanced antitumor effect [20–25]. Recently, magnetic targeting using an *in vitro* static magnetic field has been another efficient targeting strategy that induces the intravenous magnetic nanoparticles to target the disease site [26,27]. Grifantini et al. [28] investigated two drug delivery systems of super-paramagnetic nanoparticles carrying monoclonal antibody, which could be anchored at the tumor site by an external permanent magnet, thereby achieving more efficient therapeutic effect by using 200 times lower doses than free antibody doses. Using a single magnet, Martel et al. [29,30] developed the magnetic navigation system for directionally controlling magnetic carriers for effective navigation purpose. Additionally, the combination of different targeting strategies could drastically enhance the accumulation of nanoparticles in the tumor tissue compared to single-targeted strategies as mentioned in a previous report [31].

Herein, we aimed at developing a bispecific magnetic nanoprobe with broad spectrum in tumor theranostics to realize effective MRI and hyperthermia through a combined targeting strategy (Scheme 1). The dual-ligand nanoprobe was designed to specially target $\alpha_v\beta_3$ integrin commonly overexpressed on neovascular endothelium and GLUT (glucose transporter) and excessively expressed on cancer cell membrane, which has been used as the diagnostic target for tumor by positron emission tomography (PET). Hydrophobic MIONs synthesized by thermal decomposition were decorated with DSPE-PEG containing the carboxyl group and further modified with specific ligands of the c(RGDyK) peptide and D-glucosamine to form a functional molecular nanoprobe. The properties and cytotoxicity of the nanoprobes were evaluated before *in vivo* applications. More importantly, three different targeting strategies, namely, passive targeting, active targeting, and a combination of magnetic and active targeting, were compared in terms of contrast imaging effect of MRI of the tumor and antitumor efficacy of hyperthermia. Therefore, the combination strategy showed optimum effectiveness of both tumor imaging and heat treatment.

2. Materials and methods

2.1. Materials

Iron (III) acetylacetonate and N-(3-dimethylaminopropyl)-N-ethylcarbodiimide hydrochloride (EDC·HCL) were purchased from Sigma (USA). Oleylamine (OAm), oleic acid (OA), and N-hydroxysuccinimide (NHS) were obtained from Damas-Beta (China). Benzyl ether was bought from Alfa Aesar (USA). DSPE-PEG2000 and DSPE-PEG2000-COOH were obtained from A.V.T. Pharmaceutical Co., Ltd (China). c(RGDyK) peptide was purchased from ChinaPeptides Co., Ltd (China). D-glucosamine was bought from TCI (Japan).

2.2. Dual-ligand nanoprobe formulation

The magnetic iron oxide core (Fe$_3$O$_4$@OA) was synthesized by thermal decomposition of iron (III) acetylacetonate on the basis of past studies [32–34]. To compose a hydrophilic shell on the hydrophobic core, 15 mg DSPE-PEG2000-COOH and 30 mg DSPE-PEG2000 powder were dissolved in 4 ml chloroform, followed by addition of 10 mg (Fe content) iron oxide core and 6 ml deionized water. Chloroform was removed at 70 °C using a rotary evaporator to obtain mono-encapsulated Fe$_3$O$_4$@PEG, which was water-soluble. The product was further purified by magnetic separation to eliminate the empty lipid micelles and then centrifuged at 5000 rpm for 10 min to remove large aggregations.

In the synthesis of dual-ligand nanoprobe (Fe$_3$O$_4$@RGD@GLU), the prepared Fe$_3$O$_4$@PEG (10 mg, Fe content) was dispersed in 5 ml MES buffer (0.02 M, pH 5.4) by centrifugal ultrafiltration (MWCO = 100 kDa). The -COOH groups of Fe$_3$O$_4$@PEG were then activated by adding 27 mg EDC and 24 mg NHS dissolved in 2 ml MES buffer, and the mixture was vibrated for 25 min at 25 °C in a thermostatic oscillator. After activation, the intermediate was subjected to centrifugal ultrafiltration with deionized water and HEPES buffer (0.02 M, pH 7.4), and then 8 ml HEPES buffer contain-
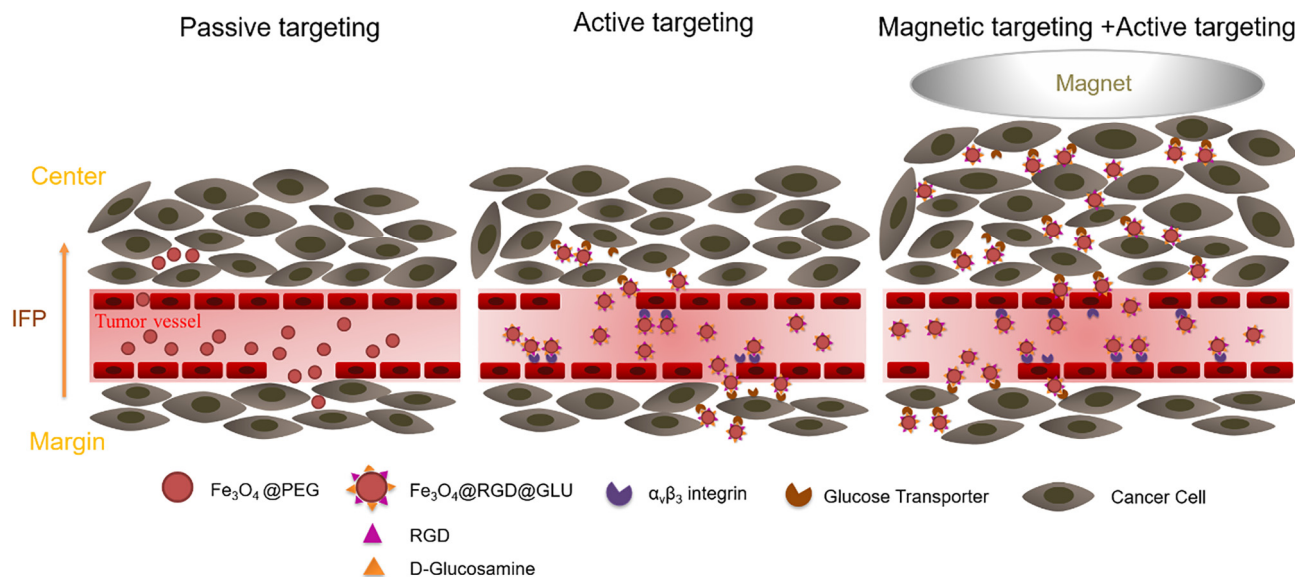
Scheme 1. Schematic diagram showing the different targeting strategies in tumor tissue.

ing 5.7 mg c(RGDyK) and 2 mg D-glucosamine was added. The reaction proceeded under vibration for 12 h at 25 °C in a thermostatic oscillator. Fe_3O_4@RGD@GLU was finally obtained by centrifugal ultrafiltration for 5 times with deionized water, and the final compound was stored at 4 °C.

2.3. Nanoprobe characterization

The morphology of hydrophobic Fe_3O_4@OA and nanoprobes of Fe_3O_4@PEG and Fe_3O_4@RGD@GLU was studied using a transmission electron microscope (TEM; JEM-200CX, JEOL, Japan). The hydrodynamic size, size distribution, and ξ-potential of the nanoprobes were measured using a nanosizer (ZS90, Malvern, UK). Their magnetic properties were evaluated in water solution by VSM (Model 7407, Lake Shore Cryotronics, USA). The concentration of the nanoprobe was determined from the concentration of iron by the 1,10-phenanthroline spectrophotometric method using a spectrophotometer (UV-3600, Shimadzu, Japan) [35]. The T_2 relaxation times of the nanoprobe were obtained using a 1.5 T MRI scanner (Avanto, Siemens, Germany), and the related r_2 relaxivity was acquired according to the slope of $1/T_2$ *vs.* concentration linear-fitting curve [36]. The heating capacity was measured in a vertical coil using an alternating current magnetic field (ACMF, 420 kHz, 2.25 kA/m) device (SPG-06-II, Shuangping, China), where the specific absorption rate (SAR) was used to evaluate the heating efficiency of the nanoprobes [37,38].

2.4. In vitro cellular interaction with nanoprobes

All the cell lines (4T1, HUVEC, and RAW 264.7) were cultured in RPMI-1640 or DMEM supplemented with 10% FBS.

Herein, 4T1 cells overexpressing GLUT were chosen to manifest the targeting ability of the nanoprobe to the surface of tumor cells, while HUVECs simultaneously expressing GLUT and $\alpha_v\beta_3$ integrin were applied to verify the bispecific binding of the nanoprobe with both cancer cells and neovascular endothelium. 4T1 cells and HUVECs were, respectively, dispersed in PBS buffer at a concentration of 10^5 cells/ml; then 200 μl cell suspension was added to every sample sink of the cell smear centrifuge. After that, the cells were fixed and underwent different processes. 4T1 cells were incubated with each of PBS, Fe_3O_4@PEG, and Fe_3O_4@RGD@GLU for 6 h in a

wet box at 37 °C, while the competing group was incubated for 2 h with free glucose, followed by 6 h incubation with addition of Fe_3O_4@RGD@GLU. The cells were rinsed with PBS after incubation, and Prussian blue staining was performed. For detecting the double specificity of the nanoprobe, HUVECs were incubated with each of PBS, Fe_3O_4@PEG, and Fe_3O_4@RGD@GLU for 6 h under the same conditions as those for 4T1 cells. Competing experiments were carried out by incubating HUVECs with each of free c(RGDyK), free glucose, and c(RGDyK) along with glucose for 2 h, and then Fe_3O_4@RGD@GLU was added for further 6 h incubation; then Prussian blue staining was performed for determining the nanoprobes on cell membranes.

For CCK8 toxicity assay, HUVECs and 4T1 cells at a density of 10^4 cells per well were incubated with Fe_3O_4@PEG and Fe_3O_4@RGD@GLU in 96-well plates for 24 h, respectively. The iron concentration of the nanoprobes varied from 20 to 100 μg/ml. Afterwards, 10 μl CCK8 was added to each well, and the plates were incubated for 1–4 h at 37 °C; the absorbance was detected at 450 nm on a microplate reader.

The anti-phagocytosis capacity of the nanoprobes was evaluated using RAW264.7 macrophages. Fe_3O_4@PEG, Fe_3O_4@RGD@GLU, and Fe_3O_4@DMSA [35] (10 nm, Fe_3O_4@OA decorated with 2,3-dimercaptosuccinic acid) were separately added to RAW264.7 cells in 6-well plates (2×10^5 cells per well) with the final iron concentration of 50 μg/ml, and the plates were incubated. After 10 h treatment, the cells were fixed and stained to validate the nanoprobes in macrophages as in our previous work [14].

2.5. Animal protocol

All animal experiments were accomplished according to Institutional Animal Care and Use Committee of Southeast University, Nanjing, China. Female mice (BALB/c, 5-week-old) were prepared for establishing breast tumor models by subcutaneous injection of 4T1 cells (2×10^6 cells in 200 μl PBS) to the upper part of the right legs. The related experiments were executed after tumor plantation for 5–8 days.

2.6. In vivo MR imaging by different targeting manners

MRI of mice tumors was performed when the tumor volume approached nearly 100 mm³. Micro-MRI equipment (PharmaScan,

Bruker, Germany) of 7.0 T was used for T_2^*-weighted imaging of the mice living body, which were divided into three groups (n = 3). Images were taken before and at different time points (3, 24, and 48 h) after intravenous dosing of Fe$_3$O$_4$@PEG, Fe$_3$O$_4$@RGD@GLU, and Fe$_3$O$_4$@RGD@GLU with a static magnetic field, respectively. The injection dosage of iron was 30 mg/kg. For the combining group of magnetic and active targeting, the button magnet with a surface magnetic intensity of 0.15 T (diameter of 12 mm and thickness of 2 mm) was placed on the tumor area before the injection. It was maintained for 4 h after injection and removed during MRI.

2.7. Iron content quantification in the main organs and tumor

The total iron content in organs was quantified using a NexION 350 inductively coupled plasma mass spectrometer. Typically, 32 female mice (BALB/c, 5-week-old) were subcutaneously injected with 4T1 cells to construct the tumor-bearing model and randomly divided into four groups (saline, Fe$_3$O$_4$@PEG, Fe$_3$O$_4$@RGD@GLU, and Fe$_3$O$_4$@RGD@GLU with a static magnetic field) when the tumor size reached 50 mm^3. The Fe$_3$O$_4$@PEG and Fe$_3$O$_4$@RGD@GLU groups were intravenously injected with MION at an iron dosage of 30 mg/kg. The Fe$_3$O$_4$@RGD@GLU with the static magnetic field group was injected with Fe$_3$O$_4$@RGD@GLU after placing a button magnet (0.15 T, diameter of 12 mm and thickness of 2 mm) on the tumor area. Twenty-four hours post different treatments, the mice were sacrificed to obtain tissue samples of the heart, liver, spleen, lung, kidney, and tumor. Then, all the tissue samples were weighed and digested in 10 ml of HNO$_3$ at 90 °C. Each digested sample was diluted with deionized water to 50 ml, and the iron content was quantified by inductively coupled plasma mass spectrometry (ICP-MS).

2.8. In vivo magnetic induction hyperthermia of tumors

The magnetic induction hyperthermia experiments began when the tumor volume reached nearly 50 mm^3. The mice were then divided into 5 groups as shown in Table 1. All treatments were operated safely under ACMF (SPG-06-Ⅱ, Shuangping, China; 450 kHz, 3.3 kA/m) every day using a bowl coil to realize tumor-

Table 1
Five different groups in hyperthermia experiments.

Group	Fe$_3$O$_4$@PEG	Fe$_3$O$_4$@RGD@GLU	Static magnetic field (Magnet)	ACMF
1	−	−	−	−
2	−	−	−	+
3	+	−	−	+
4	−	+	−	+
5	−	+	+	+

(+): yes, (−): no.

focused hyperthermia. The mice were intravenously injected with nanoprobes at a single dose of 30 mg/kg on days 0, 2, 4, 6, and 8. The treatment was performed 3 h postinjection of nanoprobes and maintained for 35 min (Scheme 2). For the 5th group, a button magnet of 0.15 T was placed on the tumor region before every injection and maintained for 4 h before thermal therapy. Thermal photographs were taken immediately after the treatment using a near-infrared thermal imager (Ti32, Fluke, USA). The average temperatures of the tumor surface were measured using SmartView4.3 software. The tumor volume was measured using a Vernier caliper and calculated using the following formula: V = AB^{2}π/6, where A represents the longer diameter and B represents the shorter one [39]. The relative tumor volume and body weight were calculated as V/V$_0$ × 100% and m/m$_0$ × 100%, where V$_0$ and m$_0$ were the initial volume and weight at the beginning of the treatment, respectively.

2.9. In vivo histological examination

For histological examination, the main organs (heart, liver, spleen, lung, and kidney) and tumors were extracted and fixed in 10% formalin after treatment on day 9, followed by paraffin embedding and slicing. First, the tissue slices of mice tumors were used for TUNEL apoptosis assay, which were stained in accordance with the manufacturer's specification. Then, the other tissue slices involving organs and tumors were used for Prussian blue and H&E staining.

2.10. Statistical analysis

The data were generally expressed as mean ± standard error. Comparisons were performed using Student's *t*-test. Values of $^*p < 0.05$, $^{**}p < 0.01$, and $^{***}p < 0.001$ were considered to have significant difference.

3. Results and discussion

3.1. Characteristics of nanoprobes

The synthesized Fe$_3$O$_4$@OA was polygonal with a uniform size of nearly 22.17 ± 1.5 nm (Fig. 1A). PEGylation with amphiphilic DSPE-PEG formed a thin shell around the magnetic core (Fe$_3$O$_4$@PEG), and further specialization with c(RGDyK) and D-Glucosamine (Fe$_3$O$_4$@RGD@GLU) caused no difference in morphology (Fig. 1B and C). As shown in Fig. 2A, the hydrodynamic size (n = 3) of Fe$_3$O$_4$@RGD@GLU (32.31 ± 0.71 nm) was similar to that of Fe$_3$O$_4$@PEG (30.86 ± 2.2 nm). A comparison of the ξ-potential of Fe$_3$O$_4$@PEG (−45.7 ± 0.96 mV) and Fe$_3$O$_4$@RGD@GLU (−30.2 ± 0.76 mV) revealed the successful conjugation of specific ligands on PEGylated nanoprobes carrying carboxyl groups (n = 4, data not shown). As RGD and glucosamine are small molecules and the amount of coupling was relatively small as compared to the whole nanoparticle, conventional detection methods such as
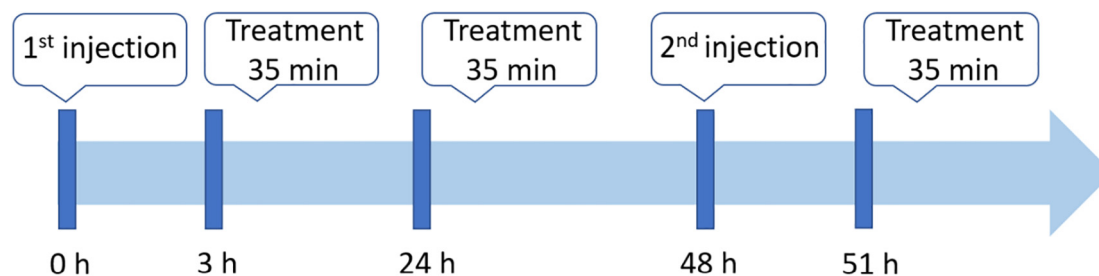
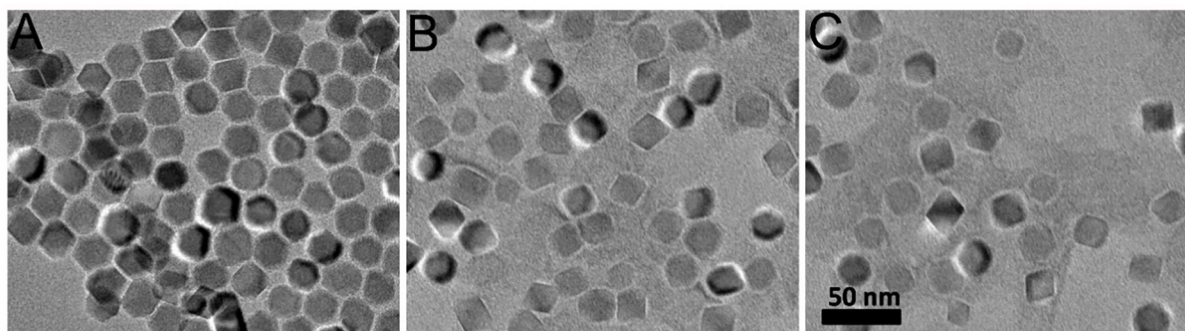**Scheme 2.** Schematic diagram of the procedure for injection and treatment.

Fig. 1. TEM images of (A) Fe$_3$O$_4$@OA, (B) Fe$_3$O$_4$@PEG, and (C) Fe$_3$O$_4$@RGD@GLU.
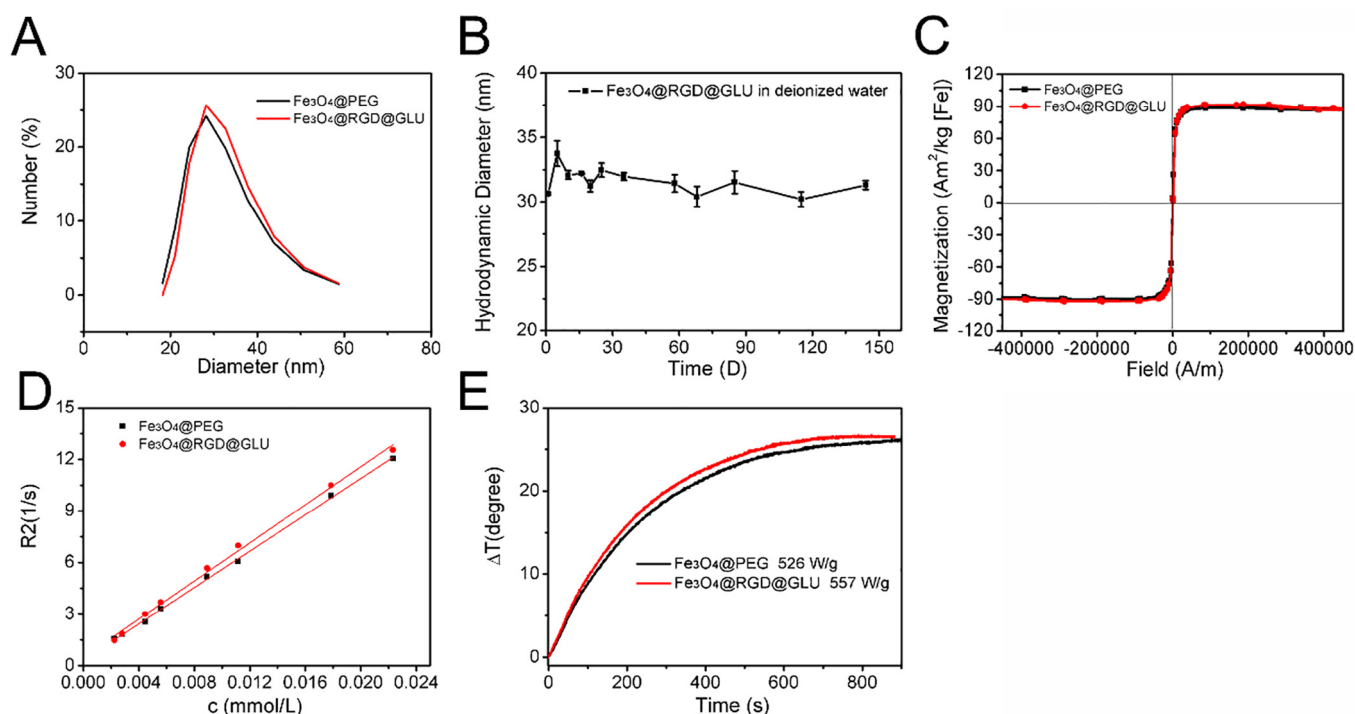
Fig. 2. (A) DLS measurement of Fe$_3$O$_4$@PEG and Fe$_3$O$_4$@RGD@GLU in water. (B) The average hydrodynamic sizes of Fe$_3$O$_4$@RGD@GLU in water within five months. The data of (B) are shown as mean ± SE (n = 3). (C) Hysteresis loops of nanoprobes measured at 300 K. (D) R2-c linear fitting curves of Fe$_3$O$_4$@PEG and Fe$_3$O$_4$@RGD@GLU measured by a 1.5 T clinic MRI scanner. (E) Heating efficiency of Fe$_3$O$_4$@PEG and Fe$_3$O$_4$@RGD@GLU tested under ACMF (420 kHz, 2.25 kA/m) at a concentration of 1 mg/ml (Fe) in aqueous solution.

Fourier transform infrared spectrometry and thermal gravimetric analysis could not qualitatively and quantitatively detect the RGD and glucosamine coupled on the nanoparticles. Furthermore, the dual-ligand nanoprobes preserved in deionized water exhibited stable size for a long time of 5 months (Fig. 2B). Both nanoprobes of Fe$_3$O$_4$@PEG and Fe$_3$O$_4$@RGD@GLU owned good magnetic properties involving relatively high saturation magnetization (M$_s$) of 90 and 91 emug^{-1} Fe with very little coercivity (2.68 and 0.99 G) and remarkable transverse relaxivity (r$_2$) of 529 and 554 mM^{-1} s^{-1}, respectively (Fig. 2C and D). This r$_2$ value was relatively high for pure iron oxide nanoparticles without doping, except one study that reported an r$_2$ value of 22 nm-sized (edge length) iron oxide nanocubes with an extremely high r$_2$ relaxivity of 761 mM^{-1} s^{-1} [40]. With the higher r$_2$ value, the larger volume would increase the uptake by the reticuloendothelial system (RES). SAR value, which is the evaluation standard of the heating ability of magnetic materials under ACMF, was reported to decrease with increasing particle concentration and increase with increasing

applied magnetic field intensity for cobalt iron oxide nanoparticles in aqueous suspension [41]. The SAR values were calculated to be 526 and 557 W/g Fe separately for nanoprobes before and after specific modification for 1 mg/ml in aqueous solution, respectively (Fig. 2E). These prominent stability and magnetisms made the dual-ligand nanoprobe an ideal contrast agent and thermo-agent for both MRI and hyperthermia treatment for the tumor.

3.2. In vitro cellular targeting, toxicity, and phagocytosis of nanoprobe

Glucose is essential for cell growth, especially for carcinoma cells based on hyper-metabolism [42]. As a result, GLUT is extensively expressed on tumor cell membranes and often used as a target for cell separation, cancer diagnosis, and therapy [43–45]. To check the binding capability of D-glucosamine modified on a dual-ligand nanoprobe to GLUT-presenting cells, both 4T1 cancer cells and HUVECs were used. As shown in Fig. 3A, the nanoprobe of Fe$_3$O$_4$@RGD@GLU could specifically target GLUT of 4T1 cells,
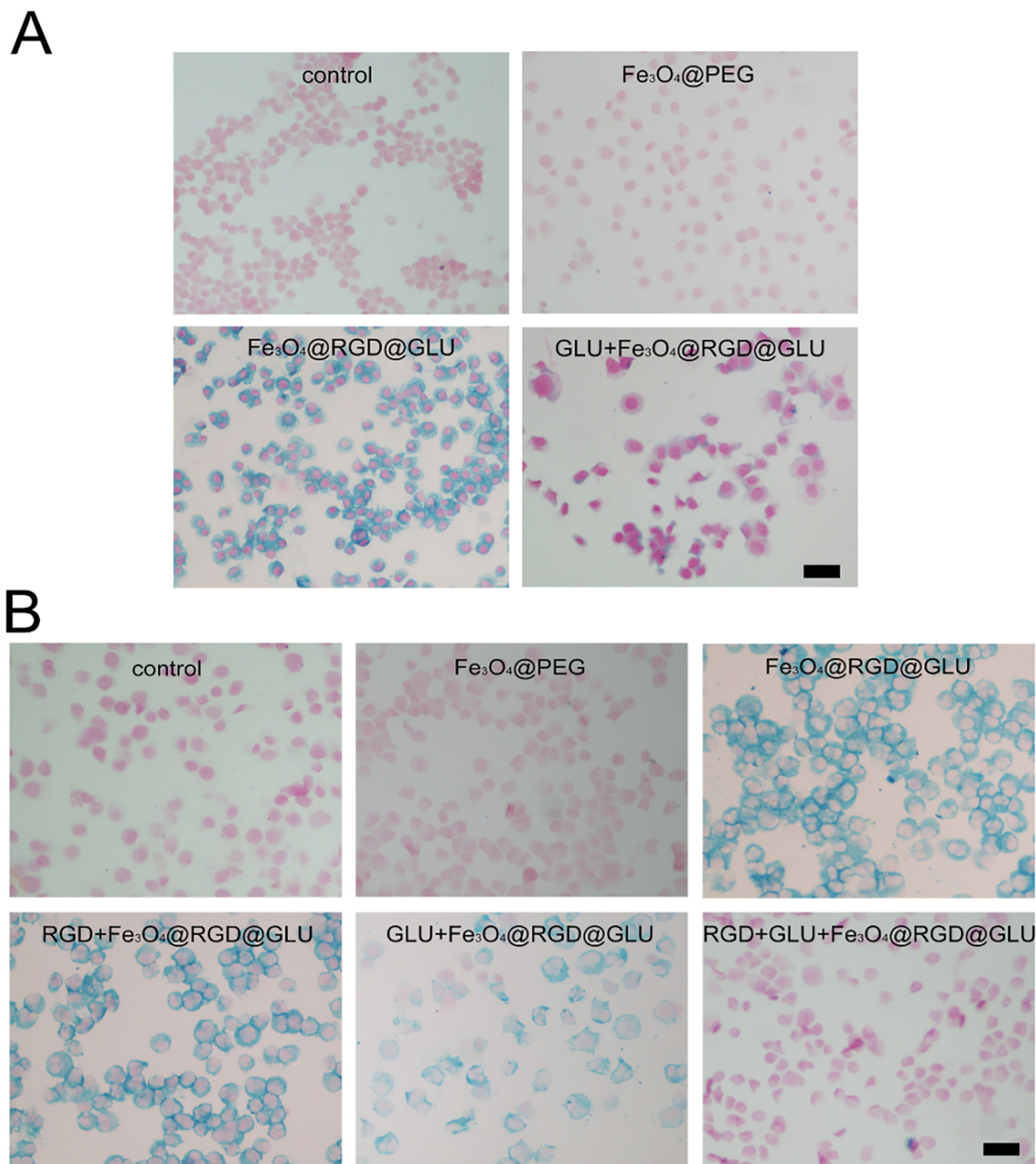
Fig. 3. Targeting ability testing of Fe$_3$O$_4$@RGD@GLU by Prussian blue staining on (A) 4T1 cells and (B) HUVECs (n = 3). For 4T1 cells incubated with PBS (control), Fe$_3$O$_4$@PEG, Fe$_3$O$_4$@RGD@GLU, and glucose (GLU) plus Fe$_3$O$_4$@RGD@GLU, respectively. For HUVECs incubated with PBS (control), Fe$_3$O$_4$@PEG, Fe$_3$O$_4$@RGD@GLU, c(RGDyK) plus Fe$_3$O$_4$@RGD@GLU, glucose (GLU) plus Fe$_3$O$_4$@RGD@GLU, c(RGDyK) plus glucose plus Fe$_3$O$_4$@RGD@GLU, respectively. The black bar represents 50 μm. (For interpretation of the references to color in this figure legend, the reader is referred to the web version of this article.)

which was qualitatively verified by Prussian blue staining (blue color). HUVECs, well known to overexpress $\alpha_v\beta_3$ integrin [46,47], were applied to demonstrate the targeting ability of c(RGDyK) on Fe$_3$O$_4$@RGD@GLU. The results shown in Fig. 3B implied that the dual-ligand nanoprobe can simultaneously adhere to GLUT and $\alpha_v\beta_3$ integrin on the cellular surface of HUVECs. We can extrapolate from the staining consequence that the expression of the GLUT protein may be superior to the expression of $\alpha_v\beta_3$ integrin on HUVECs, as the blue marking of the RGD competition experiment was relatively darker than the blue marking of the GLU competi-

tion experiment, which was the same as the result of single-targeted nanoprobes (Fe$_3$O$_4$@GLU and Fe$_3$O$_4$@RGD in Fig. S1). For flow cytometry to be performed to quantitatively check the targeting ability of the nanoprobe, the fluorescent dye needed to be decorated on nanoprobes through the carboxyl group of the particle surface, which would result in competition with RGD and glucosamine and increase the complexity of the nanoprobe. In addition, the amino group on RGD and glucosamine was the only active group, which was used to couple with the carboxyl group of nanoparticles. Thus, there was no extra active group on RGD

and glucosamine to bind to the fluorescent dye. Therefore, the targeting ability of the nanoprobe was qualitatively characterized in this study.

Iron oxide is one of the nanomaterials approved by the FDA; in addition, the coating material of DSPE-PEG2000 is also ratified to be used in clinic. Therefore, the cytotoxicity of the nanoprobes of Fe$_3$O$_4$@PEG and Fe$_3$O$_4$@RGD@GLU was really low, and the cell viability of 4T1 and HUVECs entirely exceeded 90% after 24 h cocultivation (Fig. 4A and B). These results of CCK8 assay indicated the satisfactory biocompatibility of the nanoprobes, which was suitable for *in vivo* applications.

In addition to the promotion of biocompatibility, the employment of DSPE-PEG2000 contributes to the ability of antiphagocytosis against RES. In the detection of nonspecific uptake of nanoprobes by macrophages, Fe$_3$O$_4$@DMSA was used as the control group [36]. As shown in Fig. 4C, obvious blue staining appeared in the Fe$_3$O$_4$@DMSA group when compared with the PEGylated groups of Fe$_3$O$_4$@PEG and Fe$_3$O$_4$@RGD@GLU. Despite the introduction of targeting ligands, the dual-specific nanoprobe did not induce detectable cellular uptake of RAW264.7 macrophages after 10 h of co-incubation. This result confirmed the effectiveness of PEGylation of MION [48], which makes the nanoprobes possible for use intravenously.

3.3. Contrast imaging effects of different targeting modes

It was confirmed that specific ligands coupled on iron oxide nanoparticles could effectively improve the sensitivity and efficiency of MRI for tumor when compared with the nontargeted nanoparticles in our previous research [32], which means the ligands on iron oxide nanoparticles were necessary and effective to increase the accumulation of nanoparticles in the tumor region. To further increase the accumulation of nanoparticles, magnetic targeting was added to be combined with active targeting. Thus, the experiment was conducted in three groups, namely, Fe$_3$O$_4$@PEG, Fe$_3$O$_4$@RGD@GLU, and Fe$_3$O$_4$@RGD@GLU + magnet, which was designed on a progressive basis.

To compare the distribution and accumulation of nanoprobes of several targeting modes in tumor sites, T$_2$*-weighted MRI was executed for a period of time (0–48 h). Contrast enhancement of the tumor region and the corresponding quantitative values (TNR, Tumor/Normal tissue signal Ratio [14]) are shown in Fig. 5A and B. Both the MR images and the related data demonstrated that Fe$_3$O$_4$@PEG and Fe$_3$O$_4$@RGD@GLU nanoprobes could attenuate the signal as T$_2$ contrast agents. This means that the more the nanoprobes accumulate, the darker the MR image of the tumor becomes. The favorable imaging effect occurred just 3 h post-injection of Fe$_3$O$_4$@PEG in the passive targeting group, and the contrast effect gradually receded during 24–48 h, which may be a result of the return of Fe$_3$O$_4$@PEG from the tumor tissue to vessels owing to the high interstitial fluid pressure (IFP) [49] in the tumor microenvironment. However, in the active targeting group injected with dual-ligand nanoprobes of Fe$_3$O$_4$@RGD@GLU, the tumor section achieved superior enhancement at 24 h after dosing. This phenomenon may profit from the specific ligands, which made the nanoprobes firmly attach on the tumor cells and vessel endothelium. However, in another research of dual-ligand nanoprobe for MRI, the maximum signal attenuation was produced at 6 h after injection of magnetic micelles targeting to $\alpha_v\beta_3$ integrin and human epidermal growth factor receptor-2, while a partial signal recovery was observed at 24 h postinjection [50]. The difference in MRI characteristics between the two studies may be attributed to the different surface modification and *in vivo* behavior of magnetic nanoparticles. Compared with the former two targeting modes, the combination of magnetic and active targeting yielded the best contrast effect from 3 to 48 h, which made the whole tumor region dark on the images (Fig. 5A). This optimal enhancement of tumor imaging acquired by the combination of different mechanisms was consistent with the finding obtained in the previous study [31]. It can be concluded from these results that active targeting was more sensitive and effective than passive targeting, while maximum accumulation of nanoprobes was acquired by combining multiple targeting modes, which was also helpful for further treatment of tumors such as hyperthermia.
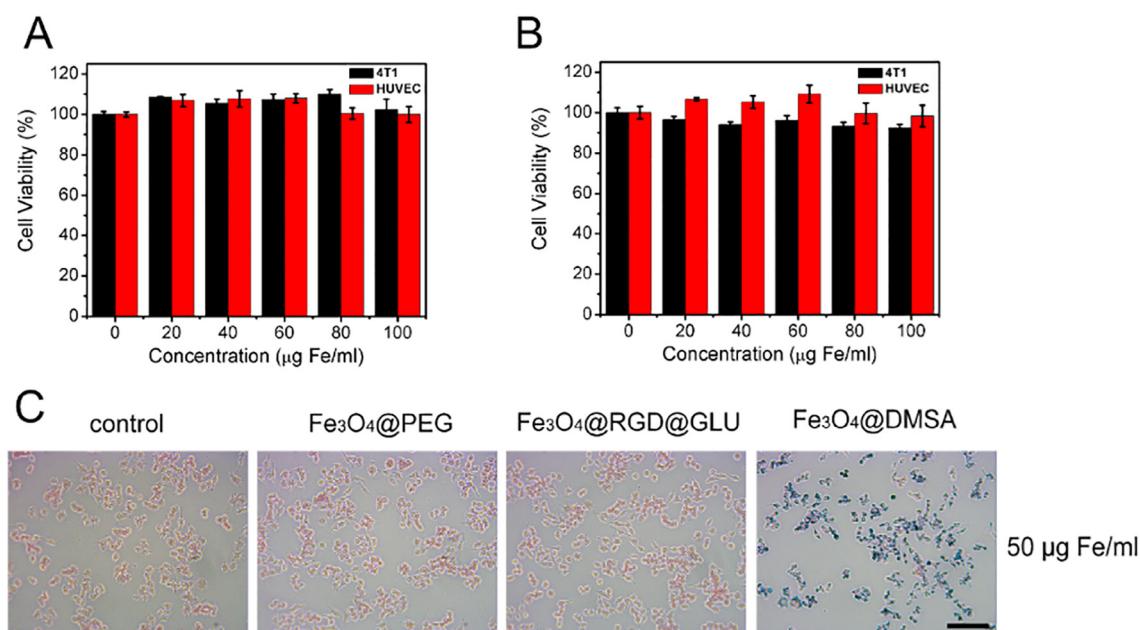
Fig. 4. Cytotoxic testing of (A) Fe$_3$O$_4$@PEG and (B) Fe$_3$O$_4$@RGD@GLU by 24 h incubation with 4T1 cells and HUVECs at different iron concentrations from 0 to 100 μg/ml (n = 4). (C) Staining images (200×) of anti-phagocytosis capacity testing of Fe$_3$O$_4$@PEG, Fe$_3$O$_4$@RGD@GLU, and Fe$_3$O$_4$@DMSA by 10 h co-cultivation with RAW 264.7 cells (n = 3). The black bar represents 100 μm.
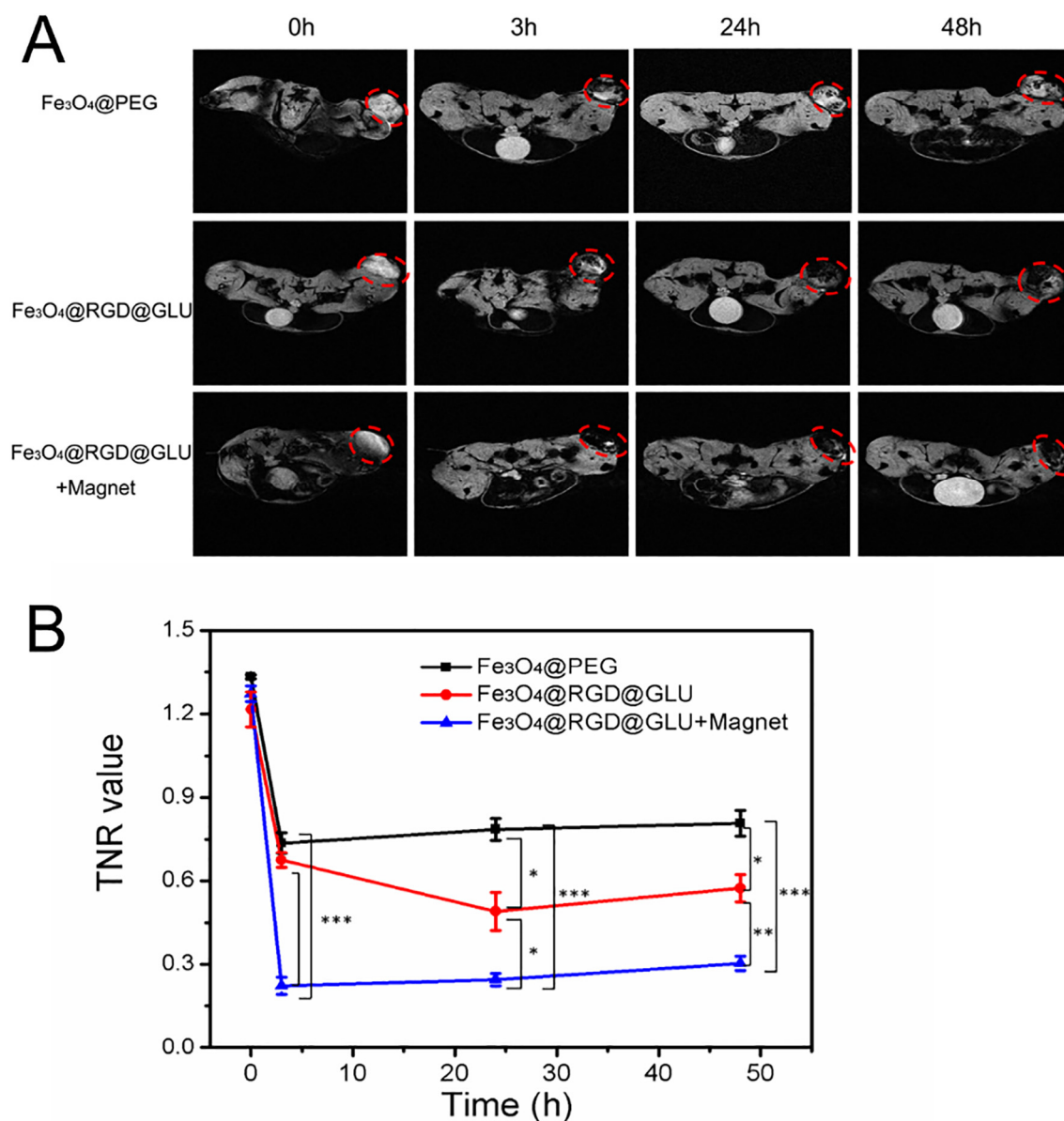
Fig. 5. (A) T_2^*-weighted MR images of mice tumors (red dotted circles displayed) gained before and at different time points after intravenous administration of Fe_3O_4@PEG, Fe_3O_4@RGD@GLU, and Fe_3O_4@RGD@GLU with an external magnetic field. (B) Quantification of tumor enhancement signals in different groups as shown in Fig (A) by TNR (Tumor/ Normal tissue signal Ratio) value. The data of (B) are shown as mean ± SE (n = 3). The asterisk indicated statistical significance ($^*p < 0.05$, $^{**}p < 0.01$, $^{***}p < 0.001$). (For interpretation of the references to color in this figure legend, the reader is referred to the web version of this article.)

3.4. Magnetic induction hyperthermia of tumors by several targeting modes

Thermotherapy is one of the important therapeutic methods for cancer treatment, wherein hyperthermia induced by magnetic nanomaterials through intravenous administration to target the tumor region received much attention. Nevertheless, it remains to be challengeable principally because of the low accumulation of thermo-agents in the tumor. As the distribution and retention time of nanoprobes in tumor sites by different targeting modes had been demonstrated through MRI as shown in Fig. 5, their anti-tumor efficiency was then compared through magnetic hyperthermia under ACMF. The tumor-bearing mice tolerated repetitive dosing of nanoprobes (five times) and daily thermotherapy (ten times) during the ten-day experiment.

The dosing strategy of injection every two days was to gain more accumulation of thermo-agents in the tumor tissue for every targeting mode. As reduplicative injection of Fe_3O_4@PEG and Fe_3O_4@RGD@GLU would cause accumulation in the liver and spleen, the minitype bowl coil was used to realize local hyperthermia focusing on the tumor site, which could dramatically minimize the influence of ACMF on the off-target organs as compared to the vertical coil used for *in vitro* SAR measurement of the nanoprobe. Further, the heating property of the nanoprobe will be relatively increased in the bowl coil (3.3 kA/m) than in the vertical coil (2.25 kA/m). The hyperthermia experiments were performed in five groups as shown in Table 1 under an ACMF condition of 1.485×10^9 Am^{-1} s^{-1}, which was far below the safe threshold of 5×10^9 Am^{-1} s^{-1} (the product of field intensity (H) and frequency (f)) [51,52]. The average temperatures of tumor surfaces monitored after hyperthermia treatment by three different targeting manners are shown in Table 2, which were approximately between 40 and 44 °C in the experimental period. In the passive targeting group, the higher temperature was mostly achieved on the day of

Table 2
Temperatures of tumors detected immediately after hyperthermia treatment.

Day	Fe_3O_4@PEG + ACMF (average temperature °C)	Fe_3O_4@RGD@GLU + ACMF (average temperature °C)	Fe_3O_4@RGD@GLU + Magnet + ACMF (average temperature °C)
0	40.8	40.7	41.3
2	41.9	42	42.7
4	41.2	42.7	43
5	40.6	43	43.1
6	41.2	42.6	43
7	40.7	42.5	43.4
8	41.7	43.2	43.2
9	41.2	42.5	43.4

injection, while no distinct increase in temperature was detected after several repetitive dosing. The temperature of the tumor region tended to be stable after three repeated injections of Fe_3O_4@RGD@GLU, which was relatively higher than the passive group.

Furthermore, it was apparent from the recorded data that the group of active targeting mode combined with the magnet gained the highest treatment temperature compared to the other two groups of either passive or active targeting. As the temperature increase (more than 39 °C) of the tumor tissue could result in cell death, the tumor growth of mice in the three groups undergoing injections and hyperthermia would be inhibited, in which the combined targeting group may have the most potential in magnetic induction thermotherapy based on the highest temperature increase on the tumor surface.

3.5. Tumor inhibition efficacy and cell death

The targeting effect of different mechanisms was further compared in tumor suppression. The representative images of tumor growth in the five groups with time are shown in Fig. 6. As the
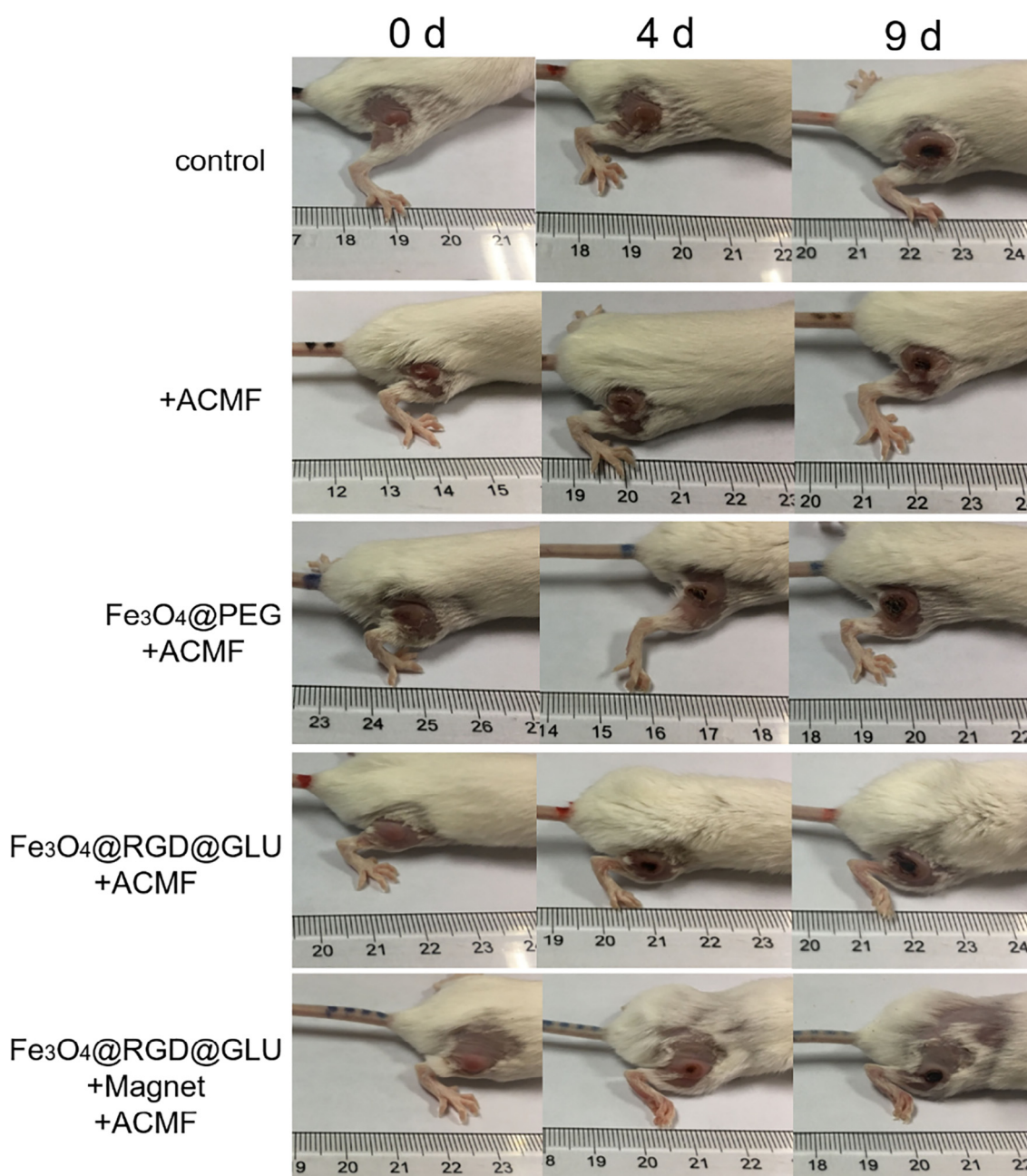

Fig. 6. Representative photographs of mice tumors of the five different groups during the 10-day experimental period.

external permanent magnet was anchored on the tumor region using a medical tape, the fur of mouse was partly torn off after a few paste and tear. As shown in Fig. 7A, the tumors on mice, which received nanoprobe-mediated hyperthermia, were obviously inhibited during the treatment cycle. Although the heating of thermo-agents in the tumor tissue produced effective antitumor efficacy in all the three groups compared with the other two control groups, the average temperatures of the tumor surfaces were slightly different. Moreover, the amounts of nanoprobes by three targeting modes were absolutely different according to the contrast imaging effect shown in Fig. 5. The accumulation of Fe_3O_4@-PEG by passive targeting on the basis of the EPR effect in the tumor was limited, and their retention time was also short, which lead to the relatively poor tumor inhibition. Active targeting by Fe_3O_4@RGD@GLU increased the amounts of thermo-agents in the tumor tissue by reducing the dependency on the ERP effect and improving their retention time in the tumor. Although the application of dual-ligand nanoprobes dramatically enhanced the MRI effect, their antitumor efficacy was not significantly improved compared with the passive one on day 8 of treatment ($p > 0.05$, Fig. 7A). In our previous study of comparing the targeting effect between passive targeting by PEGylated Mn-Zn ferrite nanocrystals and active targeting by RGD grafting, the single targeting group did not notably improve the heat induction in the tumor as compared to the passive targeting one [36]. According the review of

the literature from the past 10 years, active targeting strategies afforded delivery efficiency of 0.9% ID to a solid tumor, which was slightly higher than passive targeting strategies of 0.6% ID [53]. These data affirmed the effectiveness of active targeting strategy in enhancing the delivery ability to the tumor. However, this slight advantage may not be enough to induce a significant improvement in treatment, whereas a combination of active and magnetic targeting modes showed notable difference in tumor inhibition with other groups owing to the substantial increase in accumulation of thermo-agents at tumor sites ($p < 0.001$, Fig. 7A). We can speculate from these results that the dual-targeted strategy can increase only the sensitivity of diagnosis but not produce better therapeutic efficiency than passive targeting. Therefore, it was worth noting that the strategy of combining several targeting patterns may be more beneficial and feasible in future clinical thermotherapy by intravenous administration of thermo-agents to deliver to tumors.

As mentioned in the preceding section, temperature increase induced by mild hyperthermia would lead to cell death, therefore resulting in growth delay of tumors. To detect the cell death of each group, the tumor sections were examined by TUNEL staining after magnetic induction hyperthermia operation on day 9. The representative staining images are shown in Fig. 7B, where the cells stained brown signified apoptotic cells. In the case of passive, active, and combined groups, the ratio of apoptotic cells was,
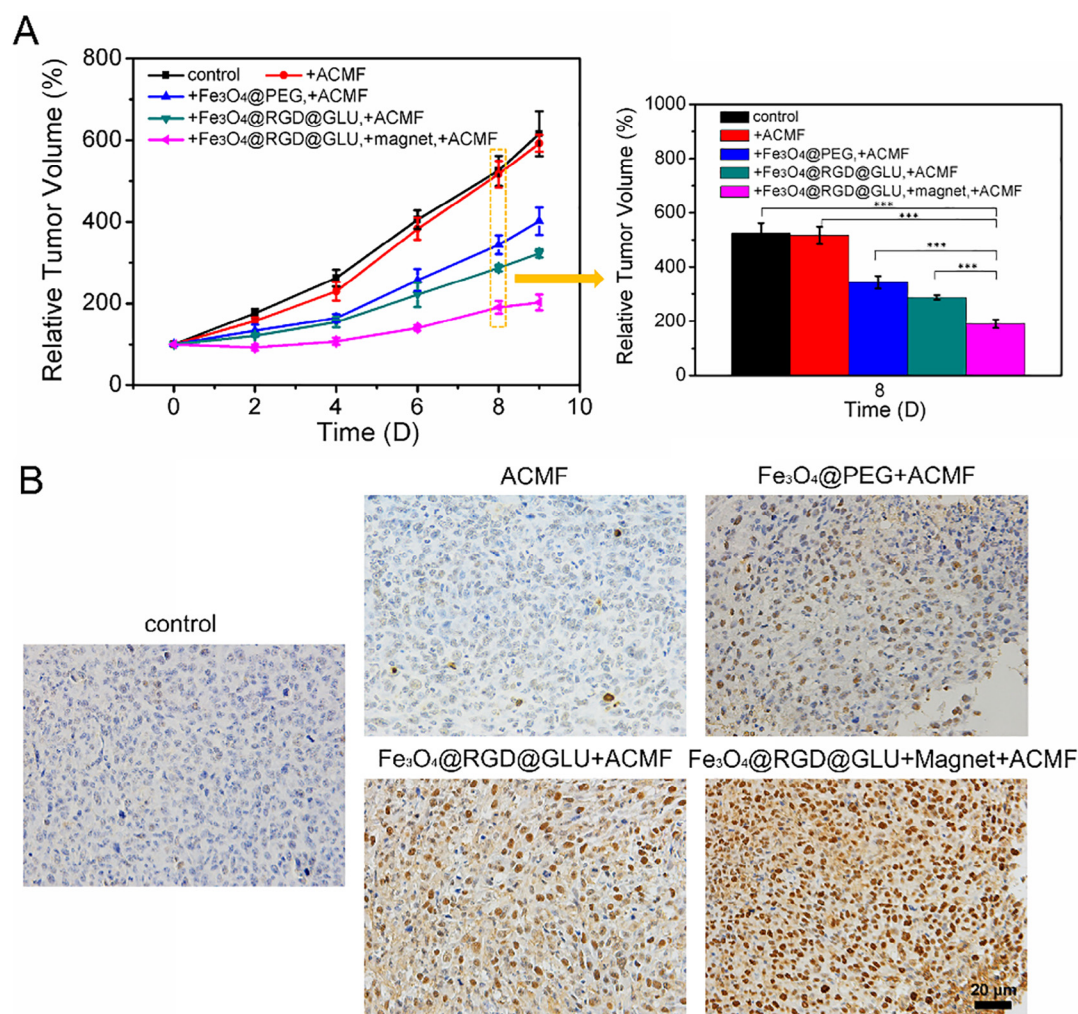
Fig. 7. (A) Tumor growth behavior of mice of five different groups with various treatments in the 10-day period. The data of (A) are shown as mean ± SE (n = 5). The asterisk indicates statistical significance (***$p < 0.001$). (B) TUNEL assay for mice tumors after various treatments on day 9.

respectively, measured as $44.5 \pm 2.16\%$, $55.26 \pm 5.43\%$, and $80.63 \pm 3.25\%$ ($n = 3$, $p < 0.05$), which was much more than the apoptotic proportion of two control groups ($1.19 \pm 0.15\%$ and $1.4 \pm 0.7\%$). These results indicated that the higher temperature increase in the tumor rendered more cell death, followed by greater tumor inhibition. Altogether, the combined targeting strategy caused maximum thermal destruction to tumor tissues.

Although tumor growth was controlled, the tumor volume was not reduced or eliminated in this study. Hyperthermia temperature is a key factor affecting the outcome of tumor treatment. Huang et al. [54] performed a single intravenous injection of iron oxide nanoparticles into tumor-bearing mice at an extremely high dosage of 1.7 g Fe/kg. The tumor was rapidly heated to ablative temperature of 60 °C by exposure to ACMF of 38 kA/m at 980 kHz. In spite of the durable ablation of tumors (78%), the condition of applied ACMF ($Hf = 37 \times 10^9$ Am^{-1} s^{-1}) was much higher than the safe threshold of 5×10^9 Am^{-1} s^{-1}. The ACMF used in this manuscript was 1.485×10^9 Am^{-1} s^{-1}, which can be appropriately enhanced to increase the heating temperature of tumor in future research. One of the great advantages of magnetic hyperthermia is no limitation of depth, but the difficulty of localizing hyperthermia on the target without producing heat damage to other organs

has always been a challenge owing to the systemic distribution of magnetic nanoparticles intravenously injected. The minitype bowl coil applied in this study could provide a general localization for thermotherapy. Recently, Tay et al. [55] reported an emerging magnetic particle imaging (MPI)-induced hyperthermia therapy, by which the spatial localization of thermal damage to the tumor was realized while minimizing the collateral damage to the nearby liver with 1–2 cm distance.
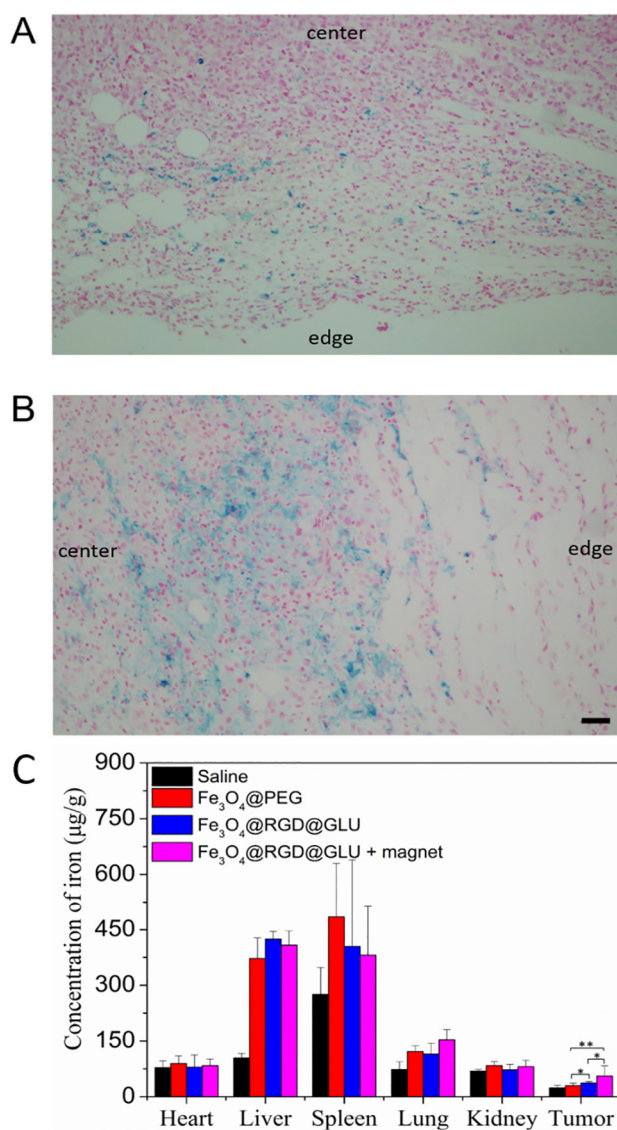
3.6. In vivo distribution of nanoprobes

Despite the feasibility of using MION for magnetic thermal therapy has been reported, a major obstacle limiting their clinical application is the insufficient accumulation at the tumor site. To clearly recognize the *in vivo* distribution of nanoprobes after multiple intravenous injections, the Prussian blue staining method was generally used. The major organs and tumors of mice from the five groups were extracted and stained for iron detection after the experimental period. As shown in Figs. 8 and S2, the magnetic nanoprobes involving Fe$_3$O$_4$@PEG and Fe$_3$O$_4$@RGD@GLU mainly accumulated in tumor tissues and organs such as liver and spleen, which inferred that the nanoprobes were metabolized through the
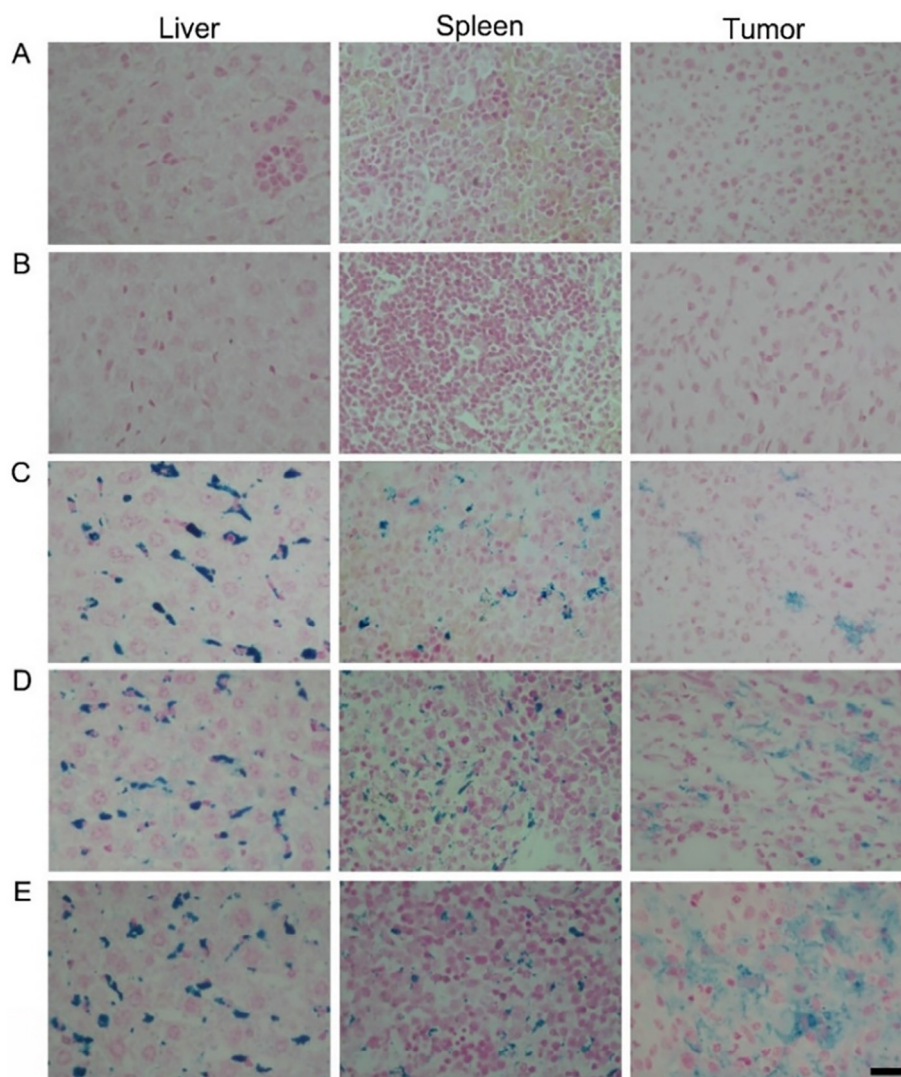
Fig. 8. Prussian blue and nuclear fast red staining images of liver, spleen, and tumor tissue sections of mice in (A) control, (B) ACMF, (C) Fe$_3$O$_4$@PEG + ACMF, (D) Fe$_3$O$_4$@RGD@GLU + ACMF, and (E) Fe$_3$O$_4$@RGD@GLU + Magnet + ACMF on day 9 after treatment. The black bar represents 50 μm. (For interpretation of the references to color in this figure legend, the reader is referred to the web version of this article.)

liver and spleen but not kidney. In spite of the similar distribution of the nanoprobes by different targeting modes, their amounts of accumulation in tumors distinctly varied. The passive agents of Fe_3O_4@PEG were inhomogeneously distributed at a relatively lower accumulation in the tumor tissue, while the dual-ligand agents of Fe_3O_4@RGD@GLU increased their cumulants in tumor by specifically targeting to both neovascular endothelium and cancer cells (Fig. 8C and D). Nonetheless, the nanoprobes of Fe_3O_4@RGD@GLU were mainly located at the tumor margin (Fig. 9A). Different from the single active targeting mode, the nanoprobes largely accumulated at the center of the tumor in the combination group (Fig. 9B). *In vivo* distributions of these nanoprobes were also quantified by the ICP-MS method, and the results (Fig. 9C) show that the total iron content of the Fe_3O_4@RGD@GLU group was significantly higher than that of the Fe_3O_4@PEG group in the tumor tissue. This result may contribute to the dual targeting ability of RGD and GLU, which can induce receptor-mediated endocytosis of the nanoprobes. Applying a static magnetic field to the Fe_3O_4@-

RGD@GLU-injected mice highly increased the iron content of the tumor tissue, demonstrating the magnetic attraction of the magnet. In accordance with Prussian blue staining results shown in Fig. 8, the distribution of iron shows high accumulation in liver and spleen. Moreover, it shows a small amount of iron accumulation in the lungs. We hypothesize that these MIONs acquire coronas that influence their clearance from the lungs.

According to the literature, the intratumor pressure is uniformly elevated because of the high permeability of vessels and the deficiency of functional lymphangion, which forms a barrier to the transport of nanomaterials [56]. This high IFP may eventually influence the theranostic efficacy of nanomedicine, which remains a challenge in tumor treatment. Herein, this problem was solved by combining magnetic targeting with dual-ligand targeting by using a static magnetic field on the surface of the tumor. The effect of an external magnet may increase the retention time of magnetic nanoprobes in tumor vessels, providing the nanoprobes more opportunities to target the specific receptors and penetrate to the tumor tissues. Despite the high pressure in 4T1 tumor, the magnetic nanoprobes were transported to the interior of the tumor under this magnetic force. This combination strategy not only increased the accumulation of nanoprobes but also enhanced their penetration depth in the tumor. In addition, *in vitro* studies verified that the movement and accumulation of magnetic nanoparticles were negatively correlated with the distance between the nanoparticles and the magnet (Fig. S5).

Although the mice received repetitive injections and hyperthermia, there was no obvious damage to their liver and spleen that accumulated numerous thermo-agents according to the result of pathological examination (Fig. S3), which could be attributed to the employment of the small bowl coil focused on the tumor region. On account of the low toxicity of iron oxide nanoprobes, Fe_3O_4@PEG- and Fe_3O_4@RGD@GLU-induced hyperthermia did not cause a remarkable decline in mice body weight, except for the combination group due to the use of magnet, which may influence the action of the mice (10% drop, Fig. S4).

4. Conclusions

In summary, a dual-ligand nanoprobe of Fe_3O_4@RGD@GLU was successfully fabricated as a theranostic agent for targeting neovascular endothelium and tumor cells. The nanoprobe possessed favorable magnetic properties and long-term stability. We have developed an effective targeting strategy that combined magnetic targeting with active targeting, which was superior to either passive or active targeting in tumor MRI and hyperthermia. This combined strategy obtained remarkable contrast enhancement effect in MRI of 4T1 tumor. Importantly, with the introduction of external magnetic targeting, the accumulation of Fe_3O_4@RGD@GLU in the tumor tissue was largely increased. In addition, the distribution of nanoprobes was also affected by the magnetic force, which promoted the transport of the nanoprobes to the interior of the tumor. Thus, the combination mode yielded best tumor inhibition compared to other targeting modes. On this basis, we hope that this dual-targeted nanoprobe would be an ideal nanomedicine as both a contrast agent and a thermo-agent for tumor diagnosis and treatment under the combination strategy.

Fig. 9. Prussian blue staining images of tumor tissue sections of (A) Fe_3O_4@RGD@GLU + ACMF and (B) Fe_3O_4@RGD@GLU + Magnet + ACMF. Edge and center represent the location on the tumor. The black bar represents 100 μm. (C) Iron content in the heart, liver, spleen, lung, kidney, and tumor tissues. Asterisk indicates statistical significance (*$p < 0.05$, **$p < 0.01$). (For interpretation of the references to color in this figure legend, the reader is referred to the web version of this article.)

Appendix A. Supplementary data

Supplementary data to this article can be found online at https://doi.org/10.1016/j.actbio.2019.07.017.

References

[1] X.H. Zhang, B.L. Liang, J. Shen, Y. Sun, A preliminary study on the influence of liver cirrhosis on the liver with Feridex-enchanced MRI, J. Pract. Radiol. 19 (3) (2003) 225–227.

[2] M. Auerbach, Ferumoxytol for the treatment of iron deficiency, Expert Rev. Hematol. 4 (4) (2011) 399.

[3] S. Vadhanraj, W. Strauss, D. Ford, K. Bernard, R. Boccia, J. Li, L.F. Allen, Efficacy and safety of IV ferumoxytol for adults with iron deficiency anemia previously unresponsive to or unable to tolerate oral iron, Am. J. Hematol. 89 (1) (2014) 7–12.

[4] B.S. Spinowitz, A.T. Kausz, J. Baptista, S.D. Noble, R. Sothinathan, M.V. Bernardo, L. Brenner, B.J.G. Pereira, Ferumoxytol for treating iron deficiency anemia in CKD, J. Am. Soc. Nephrol. 19 (8) (2008) 1599–1605.

[5] S. He, H. Zhang, Y. Liu, F. Sun, X. Yu, X. Li, L. Zhang, L. Wang, K. Mao, G. Wang, Maximizing specific loss power for magnetic hyperthermia by hard-soft mixed ferrites, Small 14 (29) (2018).

[6] N. Tran, T.J. Webster, Magnetic nanoparticles: biomedical applications and challenges, J. Mater. Chem. 20 (40) (2010) 8760–8767.

[7] S. Dutz, R. Hergt, Magnetic particle hyperthermia-a promising tumour therapy?, Nanotechnology 25 (45) (2014) 452001

[8] J.P. May, S.D. Li, Hyperthermia-induced drug targeting, Expert Opin. Drug Delivery 10 (4) (2013) 511–527.

[9] S. Kossatz, J. Grandke, P. Couleaud, A. Latorre, A. Aires, K. Crosbie-Staunton, R. Ludwig, H. Dähring, V. Ettelt, A. Lazaro-Carrillo, Efficient treatment of breast cancer xenografts with multifunctionalized iron oxide nanoparticles combining magnetic hyperthermia and anti-cancer drug delivery, Breast Cancer Res. 17 (1) (2015) 66.

[10] K. Susanne, L. Robert, D.H. Heidi, E. Volker, R. Gabriella, M. Marzia, S. Gorka, P. Vijay, F.J. Teran, H. Ingrid, High therapeutic efficiency of magnetic hyperthermia in xenograft models achieved with moderate temperature dosages in the tumor area, Pharm. Res. 31 (12) (2014) 3274–3288.

[11] R.L. Fèvre, M. Durand-Dubief, I. Chebbi, C. Mandawala, F. Lagroix, J.P. Valet, A. Idbaih, C. Adam, J.Y. Delattre, C. Schmitt, Enhanced antitumor efficacy of biocompatible magnetosomes for the magnetic hyperthermia treatment of glioblastoma, Theranostics 7 (18) (2017) 4618–4631.

[12] K.T. Jelena, D.C. Riccardo, L. Lénaic, M. Iris, G. Pablo, A.K.A. Silva, L. Nathalie, C. Olivier, F. Patrice, J.V. Singh, Heat-generating iron oxide nanocubes: subtle "destructurators" of the tumoral microenvironment, ACS Nano 8 (5) (2014) 4268–4283.

[13] K. Mahmoudi, A. Bouras, D. Bozec, R. Ivkov, C. Hadjipanayis, Magnetic hyperthermia therapy for the treatment of glioblastoma: a review of the therapy's history, efficacy, and application in humans, Int. J. Hyperthermia (2018) 1.

[14] L. Chen, F. Zang, H. Wu, J. Li, J. Xie, M. Ma, N. Gu, Y. Zhang, Using PEGylated magnetic nanoparticles to describe the EPR effect in tumor for predicting therapeutic efficacy of micelle drugs, Nanoscale 10 (4) (2018).

[15] M.A. Miller, S. Gadde, C. Pfirschke, C. Engblom, M.M. Sprachman, R.H. Kohler, K. S. Yang, A.M. Laughney, G. Wojtkiewicz, N. Kamaly, Predicting therapeutic nanomedicine efficacy using a companion magnetic resonance imaging nanoparticle, Sci. Transl. Med. 7(314) (2015) 314ra183.

[16] M.S.U. Ahmed, A.B. Salam, C. Yates, K. Willian, J. Jaynes, T. Turner, M.O. Abdalla, Double-receptor-targeting multifunctional iron oxide nanoparticles drug delivery system for the treatment and imaging of prostate cancer, Int. J. Nanomed. 12 (2017) 6973–6984.

[17] E. Doolittle, P.M. Peiris, A. Goldberg, S. Tucci, S. Rao, S. Shah, M. Sylvestre, P. Govender, O. Turan, Z. Lee, W.P. Schiemann, E. Karathanasis, Spatiotemporal targeting of a dual-ligand nanoparticle to cancer metastasis, ACS Nano 9 (8) (2015) 8012–8021.

[18] S.C. Wu, Y.J. Chen, H.C. Wang, M.Y. Chou, T.Y. Chang, S.S. Yuan, C.Y. Chen, M.F. Hou, J.T. Hsu, Y.M. Wang, Bispecific antibody conjugated manganese-based magnetic engineered iron oxide for imaging of HER2/neu- and EGFR-expressing tumors, Theranostics 6 (1) (2016) 118–130.

[19] J. Tang, L. Zhang, Y. Liu, Q. Zhang, Y. Qin, Y. Yin, W. Yuan, Y. Yang, Y. Xie, Z. Zhang, G. He, Synergistic targeted delivery of payload into tumor cells by dual-ligand liposomes co-modified with cholesterol anchored transferrin and TAT, Int. J. Pharm. 454 (1) (2013) 31–40.

[20] Y. Zhu, J. Zhang, F. Meng, C. Deng, R. Cheng, J. Feijen, Z. Zhong, cRGD/TAT dual-ligand reversibly cross-linked micelles loaded with docetaxel penetrate deeply into tumor tissue and show high antitumor efficacy in vivo, ACS Appl. Mater. Interfaces 9 (41) (2017) 35651–35663.

[21] H. Zhou, H. Xu, X. Li, Y. Lv, T. Ma, S. Guo, Z. Huang, X. Wang, P. Xu, Dual targeting hyaluronic acid - RGD mesoporous silica coated gold nanorods for chemo-photothermal cancer therapy, Mater. Sci. Eng. C Mater. Biol. Appl. 81 (2017) 261–270.

[22] S. Wang, C. Zhao, P. Liu, Z. Wang, J. Ding, W. Zhou, Facile construction of dual-targeting delivery system by using lipid capped polymer nanoparticles for anti-glioma therapy, RSC Adv. 8 (1) (2017) 444–453.

[23] C. Lin, X. Zhang, H. Chen, Z. Bian, G. Zhang, M.K. Riaz, D. Tyagi, G. Lin, Y. Zhang, J. Wang, A. Lu, Z. Yang, Dual-ligand modified liposomes provide effective local targeted delivery of lung-cancer drug by antibody and tumor lineage-homing cell-penetrating peptide, Drug Deliv. 25 (1) (2018) 256–266.

[24] W. Han, W. Yin, G. Pu, X. Chen, X. Liao, Z. Huang, Glioma targeted delivery strategy of doxorubicin-loaded liposomes by dual-ligand modification, J. Biomater. Sci. Polym. Ed. 28 (15) (2017) 1695–1712.

[25] A. Kia, J.M. Przystal, N. Nianiaris, N.D. Mazarakis, P.J. Mintz, A. Hajitou, Dual systemic tumor targeting with ligand-directed phage and Grp78 promoter induces tumor regression, Mol. Cancer Ther. 11 (12) (2012) 2566–2577.

[26] Y. Liu, F. Yang, C. Yuan, M. Li, T. Wang, B. Chen, J. Jin, P. Zhao, J. Tong, S. Luo, N. Gu, Magnetic nanoliposomes as in situ microbubble bombers for multimodality image-guided cancer theranostics, ACS Nano 11 (2) (2017) 1509–1519.

[27] Y. Qiu, S. Tong, L. Zhang, Y. Sakurai, D.R. Myers, L. Hong, W.A. Lam, G. Bao, Magnetic forces enable controlled drug delivery by disrupting endothelial cell-cell junctions, Nat. Commun. 8 (2017) 15594.

[28] R. Grifantini, M. Taranta, L. Gherardini, I. Naldi, M. Parri, A. Grandi, A. Giannetti, S. Tombelli, G. Lucarini, L. Ricotti, Magnetically driven drug delivery systems improving targeted immunotherapy for colon-rectal cancer, J. Control. Release 280 (2018).

[29] O. Felfoul, M. Mohammadi, S. Taherkhani, D.D. Lanauze, Z.X. Yong, D. Loghin, S. Essa, S. Jancik, D. Houle, M. Lafleur, Magneto-aerotactic bacteria deliver drug-containing nanoliposomes to tumour hypoxic regions, Nat. Nanotechnol. 11 (11) (2016) 941–947.

[30] S. Martel, Magnetic therapeutic delivery using navigable agents, Therapeutic Delivery 5 (2) (2014) 189–204.

[31] N. Schleich, C. Po, D. Jacobs, B. Ucakar, B. Gallez, F. Danhier, V. Preat, Comparison of active, passive and magnetic targeting to tumors of multifunctional paclitaxel/SPIO-loaded nanoparticles for tumor imaging and therapy, J. Control. Release 194 (2014) 82–91.

[32] L. Chen, J. Xie, H. Wu, F. Zang, M. Ma, Z. Hua, N. Gu, Y. Zhang, Improving sensitivity of magnetic resonance imaging by using a dual-targeted magnetic iron oxide nanoprobe, Colloids Surf B Biointerfaces 161 (2018) 339–346.

[33] J. Xie, C. Yan, Y. Zhang, N. Gu, Shape evolution of "multibranched" Mn–Zn ferrite nanostructures with high performance: a transformation of nanocrystals into nanoclusters, Chem. Mater. 25 (18) (2013) 3702–3709.

[34] H. Wu, L. Song, L. Chen, W. Zhang, Y. Chen, F. Zang, H. Chen, M. Ma, N. Gu, Y. Zhang, Injectable magnetic supramolecular hydrogel with magnetocaloric liquid-conformal property prevents post-operative recurrence in a breast cancer model, Acta Biomater. 74 (2018) 302–311.

[35] M. Song, Y. Zhang, S. Hu, L. Song, J. Dong, Influence of morphology and surface exchange reaction on magnetic properties of monodisperse magnetite nanoparticles, Colloids Surf., A 408 (16) (2012) 114–121.

[36] J. Xie, C. Yan, Y. Yan, L. Chen, L. Song, F. Zang, Y. An, G. Teng, N. Gu, Y. Zhang, Multi-modal Mn–Zn ferrite nanocrystals for magnetically-induced cancer targeted hyperthermia: a comparison of passive and active targeting effects, Nanoscale 8 (38) (2016) 16902–16915.

[37] H. Wu, L. Song, L. Chen, Y. Huang, Y. Wu, F. Zang, Y. An, H. Lyu, M. Ma, J. Chen, N. Gu, Y. Zhang, Injectable thermosensitive magnetic nanoemulsion hydrogel for multimodal-imaging-guided accurate thermoablative cancer therapy, Nanoscale 9 (42) (2017) 16175–16182.

[38] L. Chen, J. Xie, H. Wu, J. Li, Z. Wang, L. Song, F. Zang, M. Ma, N. Gu, Y. Zhang, Precise study on size-dependent properties of magnetic iron oxide nanoparticles for in vivo, Magn. Reson. Imaging (2018).

[39] H. Koichiro, N. Michihiro, S. Wataru, Y. Toshinobu, M. Hirokazu, O. Shuji, A. Masahiro, M. Toshio, I. Kazunori, Superparamagnetic nanoparticle clusters for cancer theranostics combining magnetic resonance imaging and hyperthermia treatment, Theranostics 3 (6) (2013) 366–376.

[40] N. Lee, Y. Choi, Y. Lee, M. Park, W.K. Moon, S.H. Choi, T. Hyeon, Water-dispersible ferrimagnetic iron oxide nanocubes with extremely high r_2 relaxivity for highly sensitive in vivo MRI of tumors, Nano Lett. 12 (6) (2012) 3127–3131.

[41] A.B. Salunkhe, V.M. Khot, J.M. Ruso, S.I. Patil, Water dispersible superparamagnetic cobalt iron oxide nanoparticles for magnetic fluid hyperthermia, J. Magn. Magn. Mater. 419 (2016) 533–542.

[42] I. Ak, M.P. Stokkel, E.K. Pauwels, Positron emission tomography with 2-[18F] fluoro-2-deoxy-D-glucose in oncology. Part II. The clinical value in detecting and staging primary tumours, J. Cancer Res. Clin. Oncol. 126 (10) (2000) 560–574.

[43] K. Narayanan, A.W. Lin, Y. Zheng, N. Erathodiyil, A.C. Wan, J.Y. Ying, Glucosamine-conjugated nanoparticles for the separation of insulin-secreting beta cells, Adv. Healthcare Mater. 2 (9) (2013) 1198–1203.

[44] X.H. Shan, P. Wang, F. Xiong, N. Gu, H. Hu, W. Qian, H.Y. Lu, Y. Fan, MRI of high-glucose metabolism tumors: a study in cells and mice with 2-DG-modified superparamagnetic iron oxide nanoparticles, Mol. Imag. Biol. 18 (1) (2015) 24–33.

[45] V. Mamaeva, R. Niemi, M. Beck, E. Özliseli, D. Desai, S. Landor, T. Gronroos, P. Kronqvist, I.K.N. Pettersen, E. Mccormack, Inhibiting notch activity in breast

cancer stem cells by glucose functionalized nanoparticles carrying γ-secretase inhibitors, Mol. Ther. 24 (5) (2016) 926–936.

[46] Z. Chunfu, J. Manfred, E.C. Woenne, L. Twan, M. Bernd, M.M. Mueller, Z. Hanswalter, B. Michael, E. Michael, S. Wolfhard, Specific targeting of tumor angiogenesis by RGD-conjugated ultrasmall superparamagnetic iron oxide particles using a clinical 1.5-T magnetic resonance scanner, Cancer Res. 67 (4) (2007) 1555–1562.

[47] T. Mohit, Z. Zhao, T. Jozsef, R. Erzebet, K. Margaret, E. Eva, M.T. Nakada, Multiple roles for platelet GPIIb/IIIa and alphavbeta3 integrins in tumor growth, angiogenesis, and metastasis, Cancer Res. 62 (10) (2002) 2824–2833.

[48] D. Liu, W. Wei, J. Ling, W. Song, G. Ning, X. Zhang, Effective PEGylation of iron oxide nanoparticles for high performance in vivo cancer imaging, Adv. Funct. Mater. 21 (8) (2011) 1498–1504.

[49] T.P. Padera, A. Kadambi, E. di Tomaso, C.M. Carreira, E.B. Brown, Y. Boucher, N.C. Choi, D. Mathisen, J. Wain, E.J. Mark, L.L. Munn, R.K. Jain, Lymphatic metastasis in the absence of functional intratumor lymphatics, Science 296 (5574) (2002) 1883–1886.

[50] F.M. Gong, Z.Q. Zhang, X.D. Chen, Z. Lu, X.S. Yu, Q.H. Yang, X.T. Shuai, B.L. Liang, C. Du, A dual ligand targeted nanoprobe with high MRI sensitivity for diagnosis of breast cancer, Chin. J. Polym. Sci. 32 (3) (2014) 321–332.

[51] P. Guardia, C.R. Di, L. Lartigue, C. Wilhelm, A. Espinosa, M. Garcia-Hernandez, F. Gazeau, L. Manna, T. Pellegrino, Water-soluble iron oxide nanocubes with high values of specific absorption rate for cancer cell hyperthermia treatment, ACS Nano 6 (4) (2012) 3080–3091.

[52] R. Hergt, S. Dutz, Magnetic particle hyperthermia—biophysical limitations of a visionary tumour therapy, J. Magn. Magn. Mater. 311 (1) (2007) 187–192.

[53] S. Wilhelm, A.J. Tavares, D. Qin, S. Ohta, J. Audet, H.F. Dvorak, W.C.W. Chan, Analysis of nanoparticle delivery to tumours, Nat. Rev. Mater. 1 (5) (2016) 16014.

[54] H.S. Huang, J.F. Hainfeld, Intravenous magnetic nanoparticle cancer hyperthermia, Int. J. Nanomed. 8 (1) (2013) 2521–2532.

[55] Z.W. Tay, P. Chandrasekharan, A. Chiu-Lam, D.W. Hensley, R. Dhavalikar, X.Y. Zhou, E.Y. Yu, P.W. Goodwill, B. Zheng, C. Rinaldi, Magnetic particle imaging guided heating in vivo using gradient fields for arbitrary localization of magnetic hyperthermia therapy, ACS Nano 12 (4) (2018) 3699–3713.

[56] R.K. Jain, R.T. Tong, L.L. Munn, Effect of vascular normalization by antiangiogenic therapy on interstitial hypertension, peritumor edema, and lymphatic metastasis: insights from a mathematical model, Cancer Res. 67 (6) (2007) 2729–2735.